Recognition of high-resolution optical vortex modes with deep residual learning

Jingwen Zhou,[1] Yaling Yin,[1,*] Jihong Tang,[1] Chen Ling,[1] Meng Cao,[1] Luping Cao,[1] Guanhua Liu,[1] Jianping Yin,[1] and Yong Xia[1,2,3,†]

[1]*State Key Laboratory of Precision Spectroscopy, School of Physics and Electronic Science, East China Normal University, Shanghai 200241, China*

[2]*Collaborative Innovation Center of Extreme Optics, Shanxi University, Taiyuan, Shanxi 030006, China*

[3]*NYU-ECNU Institute of Physics at NYU Shanghai, 3663 Zhongshan Road North, Shanghai 200062, China*

(Received 14 January 2022; accepted 11 July 2022; published 22 July 2022)

Optical vortex beams with fractional orbital angular momentum (OAM) can greatly enhance the channel capacity in free-space optical communication. However, high precision measurement of fractional OAM modes is always difficult, especially under the influence of atmospheric turbulence (AT). In this work, we identify the high-resolution OAM modes down to 0.01 using an improved residual neural network (ResNet) architecture based convolutional neural network (CNN). Experimentally, using a single cylindrical lens, the light intensity distribution can be readily converted into a diffraction pattern containing significant features trained into a CNN model. For the fractional OAM modes from 5.0 to 5.9 over a long propagation distance of 1500 m, at 0.1 resolution, our model's predicting accuracy is up to 99.07% under strong AT, $C_n^2 = 1 \times 10^{-15}$ $m^{-2/3}$. At 0.01 resolution, the accuracy is as high as 86.98% under intermediate AT, $C_n^2 = 1 \times 10^{-16}$ $m^{-2/3}$, and exceeds 73.78% under strong AT, $C_n^2 = 1 \times 10^{-15}$ $m^{-2/3}$. So, these results may have great implications in free-space optical communication.

DOI: 10.1103/PhysRevA.106.013519

I. INTRODUCTION

About 30 years ago, Allen and co-workers showed that a Laguerre-Gaussian beam carries a well-defined orbital angular momentum (OAM) of light [1]. The OAM of the optical vortex (OV) beam is related to a helical phase front, which can be expressed by a transverse phase structure of $\exp(-il\varphi)$, where φ is the azimuthal angle and l is the topological charge [2–4]. Application of this kind of "structured light" has impacted the fields, such as quantum optics [5,6], optical trapping [7,8], optical imaging [9], and nonlinear optics [10], among many others [11]. Particularly, the OAM has an infinite range of possibly achievable modes, which can be used in information transmission—a hot topic in optical communication [12–16].

As is known, both the growing phase singularity and the diffraction effect have great influence on the intensity distributions of a vortex beam. So, many factors, e.g., more OAM states, smaller phase singularities, and better resolution of the OAM mode with different topological charge, will determine the communication capacity. For example, if the interval between adjacent topological charges is 0.01 (namely the resolution of OAM), the fractional OAM modes can then be expanded 100 times comparing to the adjacent integer one. So, the fractional OAM can greatly increase the capacity of communication channels. An evolutional vortex structure of noninteger OAM modes, whose annular intensity profile has the radial dark gap, was theoretically studied by Berry in 2004 [17]: The noninteger OAM beams can be described as a superposition of a series of Fourier series, $\exp(il\phi) = \frac{\exp(i\pi\alpha)\sin(\pi\alpha)}{\pi} \sum_{-\infty}^{\infty} \frac{\exp(in\phi)}{\alpha - n}$, where α is a fractional value, and n is an integer. Meanwhile, the fractional OAM beam being hosted within a converted Gaussian beam was analyzed experimentally for both phase and intensity distribution [18]. Likewise, the half integer l revealing a line of alternating charge vortices near the radial dislocation was observed by Leach *et al.* [19]. The generation and precision measurement of OAM modes with fractional topological charges turns out to be very beneficial in the OAM-based free-space optical communication (OAM-FSOC) [20–28]. As such, various methods have been developed to measure the fractional topological charges of OAM modes, such as the fork grating [20], the interferometer structure [21,22], the dynamic angular double slits [23], the OAM sorting method [24,25], the cylindrical lens [26], and the multifocal array [27]. The best resolution and accuracy of OAM modes with the fractional topological charges, as reported so far, are 0.1 and 97.86%, respectively.

On the other hand, machine learning can lead to high accuracy in image recognition, where a number of images are used as the training set to improve model performance for future prediction [29]. Due to the advanced multilayer learning, convolutional neural networks (CNNs) are good at recognizing raw images through discovering intrinsic features of input images [30]. Recently, several effective methods have been able to obtain the accurate recognition for the OAM modes by combination of neural networks with different physical models. In 2017, Doster *et al.* proposed using CNN with an AlexNet framework to classify and recognize OAM beam intensity patterns affected by atmospheric turbulence: More

*ylyin@phy.ecnu.edu.cn
†yxia@phy.ecnu.edu.cn

than 99% accuracy was achieved [31]. In 2019, Liu *et al.* performed a deep learning method with a DenseNet framework to recognize the fractional OAM modes: A resolution of 0.01 with 98% accuracy on 10 000 images was achieved [32]. In 2021, Na *et al.* reported to recognize the OAM mode with 0.03 resolution for higher than 99%; transmitted images with correlations were higher than 0.99 and the error rate was lower than 0.1% [33].

Furthermore, several reports proved that the OAM beams can be successfully transmitted over long distance, revealing the potential application in OAM-FSOC. In 2012, twisted radio waves were performed over 420 m in Venice [34]. In 2014, Vallone *et al.* transmitted the single photons with OAM information over 210 m in a large hall in Padua, Italy [35]. In the same year, Krenn *et al.* reported that the information encoded by 16 different spatial modes was successfully transmitted over a 3-km intracity link across Vienna [13]. In 2015, Lavery *et al.* studied turbulence induced orbital angular momentum channel crosstalk over 1.6 km [36]. In 2016, Krenn *et al.* achieved twisted light transmission over 143 km [37]. As the distance of propagation increases, the beam profiles are subject to attenuation, diffraction, atmospheric turbulence, or any other noise, and so require the help of CNN [13,37].

Herein, we report results to achieve higher precision recognition on higher resolution OAM modes under atmospheric turbulence (AT) over long distance [26,31–33]. Experimentally, a single cylindrical lens with the fractional phase hologram is used to acquire good quality of experimental data containing the stable, reliable, and quantitative recognition features, such as the number of stripes and points (or gaps) in the vortex modes. Theoretically, the CNN based ResNet50 model is used to perform deep learning. A lab-simulated AT is incorporated as well. For 0.1 resolution at $z =$ 1500 m, we achieve 100% accuracy under weak AT, $C_n^2 = 1 \times 10^{-17}$ m$^{-2/3}$, and more than 99% accuracy under strong AT, $C_n^2 = 1 \times 10^{-15}$ m$^{-2/3}$. For 0.01 resolution at $z = 1500$ m, we achieve more than 97% accuracy under weak AT, and more than 73% under strong AT.

II. EXPERIMENTAL SETUP

Figure 1 shows the experimental setup for generation and measurement of fractional OAM modes. We use a highly stable HeNe laser with a center wavelength of 632.991 nm to generate the fractional OV beam. The beam is incident onto a spatial light modulator (SLM), which preloads the phase plane, helical phase front, AT, and cylindrical lens information. In our experiment, the SLM (Holoeye) is a phase-only reflective liquid crystal device with 1920 × 1080 pixels and 8.0 μm per pixel pitch. To simulate the long distance propagation, we superpose two, four, and six layers of phase screens with the adjacent distance $\Delta z = 250$ m. We change the intensities of AT from weak ($C_n^2 = 1 \times 10^{-17}$ m$^{-2/3}$) to strong ($C_n^2 = 1 \times 10^{-15}$ m$^{-2/3}$) to simulate the AT propagation at 500, 1000, and 1500 m for the OAM spanning from 5.0 to 6.0 (0.1 resolution) and from 5.00 to 5.10 (0.01 resolution). The diffraction patterns are acquired by a charge-coupled device (CCD) camera, and the CNN model extracts the image features to achieve high accuracy identification.

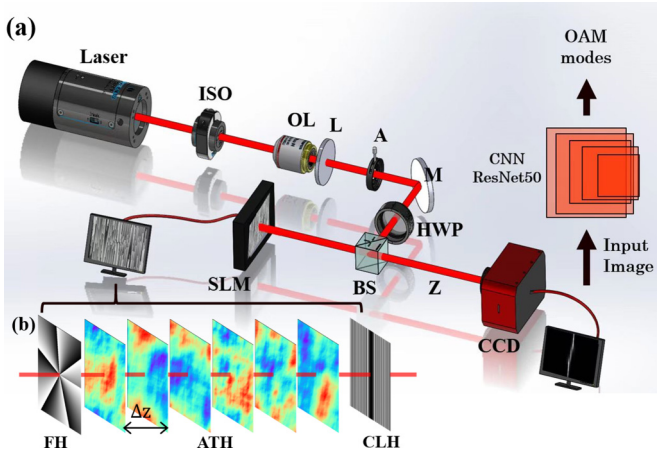

FIG. 1. (a) Experimental setup for fractional OAM modes. ISO: Optical isolator; OL: Objective lens; A: Aperture; L: Lens; M: Mirror; HWP: Half wave plate; BS: Beam splitter; SLM: Spatial light modulator; CCD: Charge-coupled device; z: The distance between SLM and CCD. (b) Generation of the hologram on SLM. FH: The fractional phase hologram of OAM mode $l = 5.50$; ATH: The atmospheric turbulence hologram; CLH: The cylindrical lens phase hologram with a focal length of $f = 0.3$ m.

III. INTENSITY DISTRIBUTION OF OV BEAMS WITH A CYLINDRICAL LENS

The OV beam can be easily converted by loading a spiral wave-front phase at Gaussian beams using a spiral light modulator. Instead of using the Laguerre Gaussian beam mentioned in the usual method [38,39], we use the modulated Gaussian beam for simulating and experimenting. The OV beam field distribution can be written as

$$E(r,\varphi) = A\exp\left(-\frac{r^2}{\omega_0^2}\right)\exp(il\varphi), \tag{1}$$

where (r,φ) denotes the cylindrical coordinates, and A and ω_0 are the complex amplitude and the waist of the incident Gaussian beam, respectively.

The method to convert diffraction patterns by cylindrical lens is based on the astigmatic transformation of strongly deforming the vortex core into titled dark stripes, which can reflect the number of topological charges [26,40–42], and the OV beams can be constructed by the cylindrical-lens phase function,

$$\psi = k(f - \sqrt{f^2 + x^2}) \tag{2}$$

where x denotes the Cartesian coordinates, $k = 2\pi/\lambda$, and f represents the focal length of the cylindrical lens. Based on the Fresnel diffraction integral, as follows, the field distribution on the focal plane of the cylindrical lens is

$$E(\rho,\theta,z) = \frac{\exp(ikz)}{i\lambda z}\int_0^\infty\int_0^{2\pi} E(r,\varphi)\exp(i\psi) \times \exp\left(\frac{ik}{2z}[r^2+\rho^2-2\rho r\cos(\varphi-\theta)]\right) r dr d\varphi. \tag{3}$$

The diffraction images of fractional OAM beams with a resolution of 0.1 (from $l = 5.0$ to $l = 6.0$) and 0.01 (from

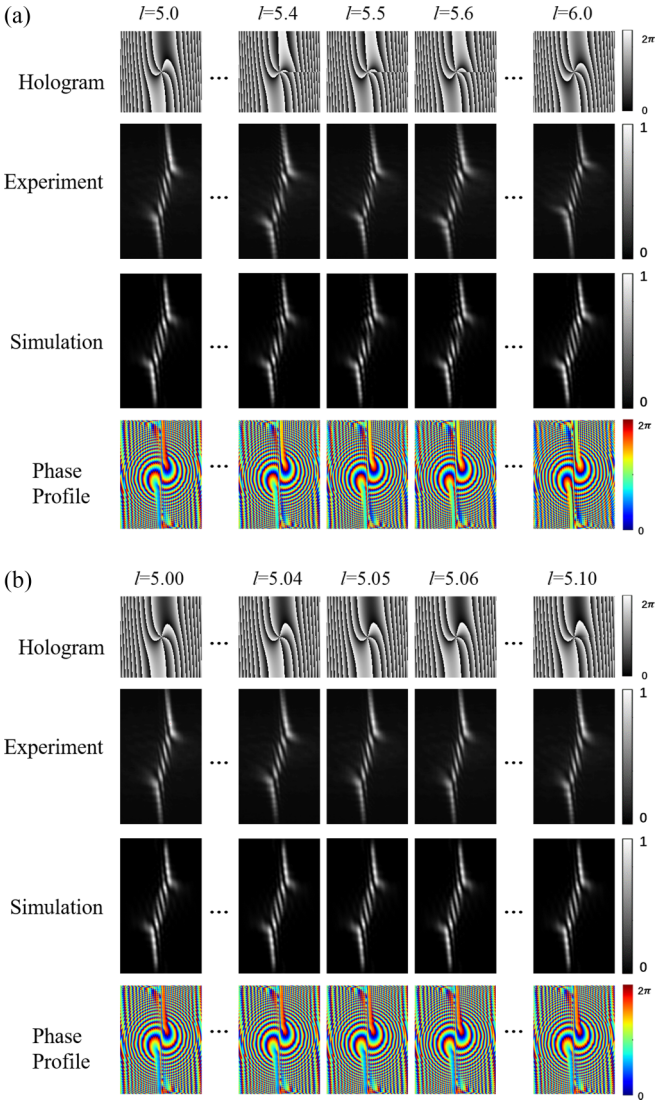

FIG. 2. (a) For 0.1 resolution. (b) For 0.01 resolution. Horizonal: The holograms with OAM and cylindrical phase information (focal length of $f = 0.3$ m), experiment and simulation (the normalized optical intensity distribution at the focal plane of cylindrical lens), and the phase distribution of the OAM beam. Vertical: According images at different l.

$l = 5.00$ to $l = 5.10$) are shown in Figs. 2(a) and 2(b), respectively. The first row shows the phase holograms containing fractional OAM and cylindrical phase information with a focal length of the cylindrical lens $f = 0.3$ m. The second and third rows show the experimental and simulated normalized optical intensity distribution at focal plane of cylindrical lens, respectively. The fourth row shows the phase distribution of the OAM beam.

From the experiment results in Fig. 2(a), for $l = 5.0$, we can see five dark stripes, which are equal to the topological charges being sandwiched between the bright stripes. As l increases with 0.1 resolution, the third bright strip (from top), starting from $l = 5.0$, is gradually divided into bifurcation which is quite clear at $l = 5.4$. While l is 5.5 to 5.6, the bright stripe of bifurcate is continually getting bigger. Finally, at $l = 6.0$, the bifurcate separates into two new bright stripes, appearing six dark stripes in total—equal to the topological charges. The simulated results agree well with the experiment.

The phase profiles in the fourth row show the phase evolution of beams with different l. The dark blue area in phase profiles denotes the zero phase. Compared with the phase profile of $l = 5.0$, whose center has a five-spiral pattern, each represents a phase from 0 to 2π, and the phase profile of $l = 6.0$ changes to six period with 0–2π phase in the center part. However, in Fig. 2(b), when l changes with an interval of 0.01, it is hard to see the clear difference among each category of images, which will be instead captured by the CNN model.

IV. CONSTRUCTION OF PHASE SCREENS ON AT

During the propagation of the beam, AT with random distribution will severely distort the helical phase front and destroy the structure of the OV beam, which can make an arbitrary addition difficult in the OAM communication link. Here, we use the Hill-Andrews model, a modified Kolmogorov-based spatial spectrum, to simulate the atmospheric turbulence [43]. The atmospheric refractive index variation spectrum can be expressed as

$$\Phi_n(k) = 0.033C_n^2\left[1 + 1.802\sqrt{\frac{k^2}{k_l^2}} - 0.254\left(\frac{k^2}{k_l^2}\right)^{7/12}\right] \times \frac{\exp\left(-\frac{k^2}{k_l^2}\right)}{\left(k_0^2 + k^2\right)^{11/6}} \tag{4}$$

where k^2 is $k_x^2 + k_y^2$, k_x^2, k_y^2 is the frequency wave spectrum data, $k_l = 3.3/l_0$, $k_0 = 2\pi/L_0$, and l_0 and L_0 are the inner and outer scale of AT, respectively. C_n^2 is the structure constant of the refractive index, describing the intensity of AT [44]. According to the value C_n^2, the turbulence conditions can be divided into three categories: Weak, intermediate, and strong [45].

The spatial variation in AT can be approximated by several phase screens that modify the phase profile upon the beam propagation. The relationship between the spatial variation of the phase screen $\sigma^2(k)$ in Cartesian coordinate and refractive index variation spectrum $\Phi_n(k)$ can be written as follows [46]:

$$\sigma^2(k) = \left(\frac{2\pi}{N\Delta x}\right)^2 2\pi k_z^2 \Delta z \Phi_n(k), \tag{5}$$

where Δx is the grid spacing of random phase screen and N is the size of the phase screens. $k_z = 2\pi/\lambda$, and Δz is the interval distance between adjacent phase screens. Then, the phase screen in the frequency domain can be represented by fast Fourier transform operation,

$$\xi(k) = \mathrm{FFT}(M\sigma(k)), \tag{6}$$

where FFT ( ) describes the fast Fourier transform and M represents a complex Gaussian random matrix; in the frequency domain, the mean value is 0 and the variance is 1.

The layered model for turbulence is typically used when light propagates between layers [47]. The statistically generated phase screens at each layer represent the phase that would have occurred in propagation through turbulence from previous layers. The Kolmogorov spatial spectrum is used to

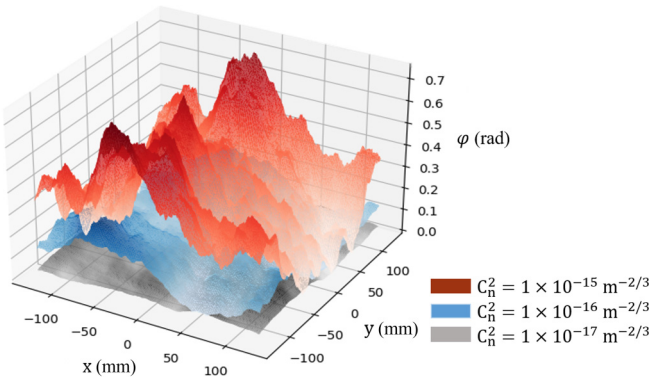

FIG. 3. Random AT phase perturbation caused by one layer of phase screen (Δz 250 m) at $C_n^2 = 1 \times 10^{-17}$ m$^{-2/3}$ (in grey), $C_n^2 = 1 \times 10^{-16}$ m$^{-2/3}$ (in blue), $C_n^2 = 1 \times 10^{-15}$ m$^{-2/3}$ (in red).

generate phase screens for the turbulent medium. The phase information of each layer in the process of beam propagation can be designed to generate and superimpose on a spatial light modulator. With the decrease in Δz, the amount of computation will be greatly increased.

Figure 3 shows the random phase perturbation of one phase screen of AT with the parameter $\Delta z = 250$ m. The inner and outer scale of AT is configured as $l_0 = 0.01$ m and $L_0 = 100$ m. The gray is for weak turbulence with $C_n^2 = 1 \times 10^{-17}$ m$^{-2/3}$, the blue is for intermediate $C_n^2 = 1 \times 10^{-16}$ m$^{-2/3}$, and the red is for strong $C_n^2 = 1 \times 10^{-15}$ m$^{-2/3}$.

To do proper computing (GPU: NVIDIA, RTX-3070; CPU: Intel, i7-10700), we take $\Delta z = 250$ m to simulate AT at 500, 1000, and 1500 m, which superpose 2, 4, and 6 times of Δz, respectively.

Figure 4 shows the intensity distribution of each fractional OAM beam with 1500-m AT propagation for three C_n^2 values, 1×10^{-17} m$^{-2/3}$ in rows of (a) and (b), 1×10^{-16} m$^{-2/3}$ in rows of (c) and (d), and 1×10^{-15} m$^{-2/3}$ in rows of (e) and (f). The rows of (a), (c), and (e) are detected by CCD without the cylindrical lens, and the rows of (b), (d), and (f) are detected by CCD at the focal plane of the cylindrical lens. Compared to the images in rows (a) and (c), the images in row (e) are more severely distorted from the turbulence. However, due to the diffraction by a cylindrical lens, the fractional OAM modes, seen in rows (b), (d), and (f), better preserve the original features from the turbulence in that the dark and light stripes can still be well recognized. It may be because that the cylindrical lens can converge beams in one direction (x axis), and both the fractional OAM modes and the atmospheric turbulence are compressed at the same time, coincidently reducing the influence of AT onto the light field distribution.

V. ARCHITECTURE OF CNN MODEL

The ability of image feature extracting, which can be greatly enriched by increasing the number of stacked layers (depth of network), is one of the most important evaluated parts among all the CNNs. However, the deeper the networks are, the more difficult the training will be [48,49]. Compared with several typical CNN models, AlexNet and VGG, we finally chose the ResNet model algorithms because they can not only capture all the subtly and breadth, but also obtain the high recognition accuracy. The ResNet50 model is shown in Fig. 5, which innovatively puts the residual function into the fundamental framework to ease the training of networks and considerably increase the depth [50]. In brief, for raw images of 224 × 224 pixels as input, the image is processed first by Conv1 with 7 × 7 convolution kernels and a maxpooling layer. Then, there are four "bottleneck" building blocks, a deeper residual function; each of them has a three-layer stack of 1 × 1, 3 × 3, and 1 × 1 convolution. After the residual blocks, the information is transmitted into an average pooling layer, a

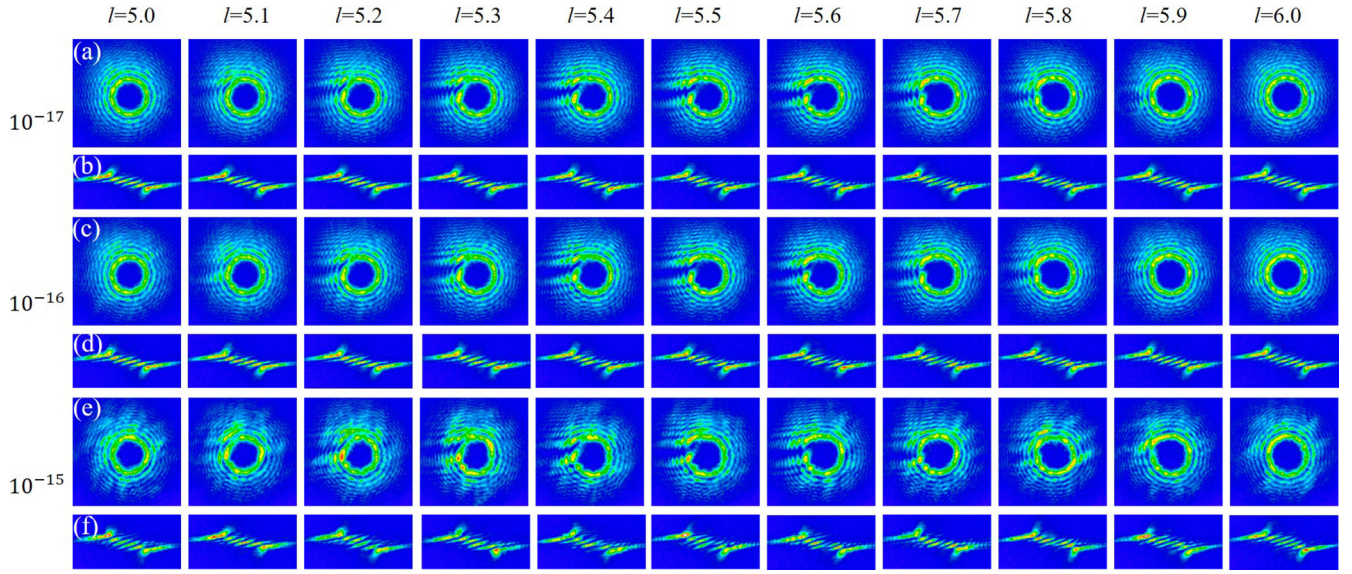

FIG. 4. Intensity distribution of the fractional OAM beams transmitted over 1500 m AT channels with different C_n^2: 1×10^{-17} m$^{-2/3}$, 1×10^{-16} m$^{-2/3}$, 1×10^{-15} m$^{-2/3}$. Rows (a), (c), (e): Detected by CCD without the cylindrical lens. Rows (b), (d), (f): Detected by CCD at the focal plane of the cylindrical lens.

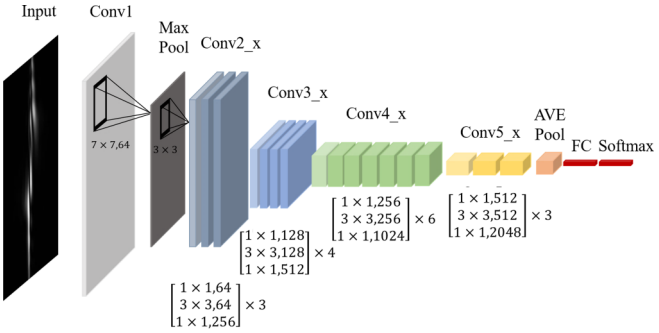

FIG. 5. Image recognition of fractional OAM based on the ResNet50 architecture used in CNN model.

fully connected (FC) layer, and finally a softmax function for classification.

We use about 15 000 images for 0.1 resolution, and 60 000 images for 0.01 resolution. The ratio of training, validation, and test sets is 6 : 2 : 2. The accuracy and loss function curves are shown in Fig. 6 for images at the intermediate $C_n^2 = 1 \times 10^{-16}$ m$^{-2/3}$ plus $z = 500$ m. From Fig. 6, we can clearly see that loss function and accuracy are well converged at $C_n^2 = 1 \times 10^{-16}$ m$^{-2/3}$, $z = 500$ m. For the resolution 0.1, the accuracy is nearly 100% after only 15 epochs, and the loss value is almost 0 after epoch = 10, demonstrating that the ResNet model has a good mapping relationship between input and output. For the resolution 0.01, the accuracy is nearly 92.74% after 25 epochs, and the loss value is almost 0 after 20 epochs. Besides, at $C_n^2 = 1 \times 10^{-16}$ m$^{-2/3}$, $z =$ 1000 m, the loss function and accuracy curves hold steady after epoch = 15 at 0.1 resolution and epoch = 20 at 0.01 resolution. At $C_n^2 = 1 \times 10^{-16}$ m$^{-2/3}$, $z = 1500$ m, the accuracy curve of 0.1 resolution turns to be stable within 15 epochs and the loss faction is well converged within only 10 epochs, while the accuracy curve of 0.01 resolution remains steady after 25 epochs and the loss function well converged after 20 epochs. The confusion matrix shows that the iteration number epochs = 50 is enough for the loss function to converge to the high accuracy, which shows that our model has been suitably trained. In addition, the results show that data preprocessing can maintain the model stability.

VI. RESULTS AND DISCUSSION

A. Classification of OAM for 0.1 resolution

To classify OAM for 0.1 resolution, we randomly combine the influences of the intensity of AT (1×10^{-17} m$^{-2/3}$, 1×10^{-16} m$^{-2/3}$, $C_n^2 = 1 \times 10^{-15}$ m$^{-2/3}$) and the propagation distance (500, 1000, 1500 m). We collected about 15 000 images. Then, we used 3000 images (not in the training set) for test accuracy and confusion matrix. As shown in Fig. 7, the black points represent a short propagation distance ($z = 500$ m), red ones represent a medium propagation distance ($z = 1000$ m), and blue ones represent a long propagation distance ($z = 1500$ m).

With the increase in propagation distance, obviously the phase perturbation gets stronger, so the accuracy declines but modestly in our model. At weak $C_n^2 = 1 \times 10^{-17}$ m$^{-2/3}$ and $z = 500$ m, the test accuracy is almost 100% at all three

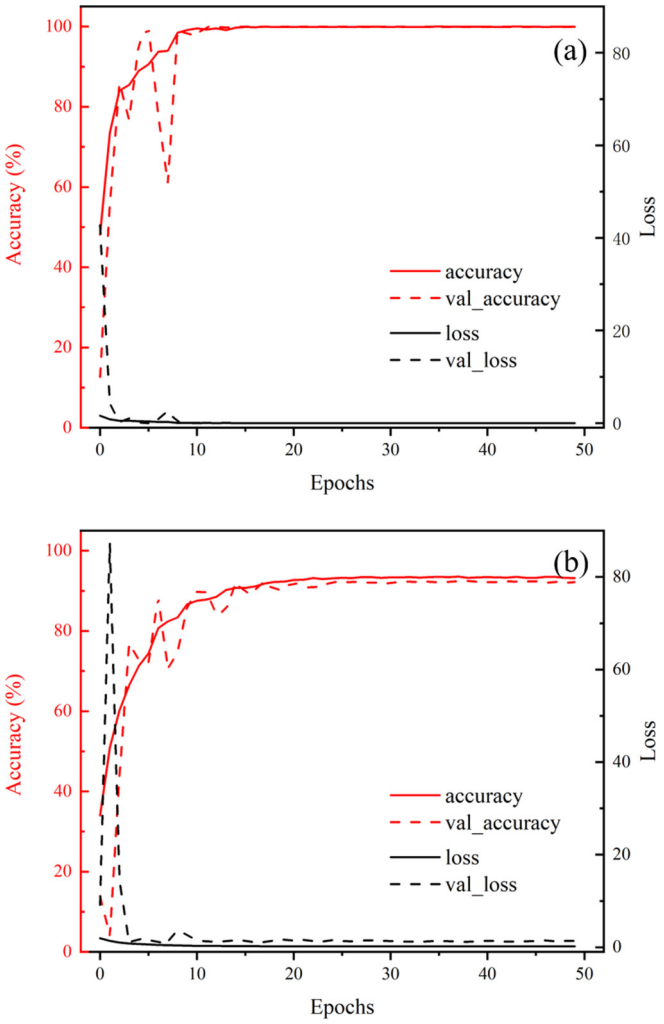

FIG. 6. Accuracy and loss function curves at $C_n^2 = 1 \times 10^{-16}$ m$^{-2/3}$, $z = 500$ m. (a) For 0.1 resolution. (b): For 0.01 resolution. Red curves are for accuracy and black curves are for error reduction upon iterations. Solid lines are from training set and dotted lines are from validation set.

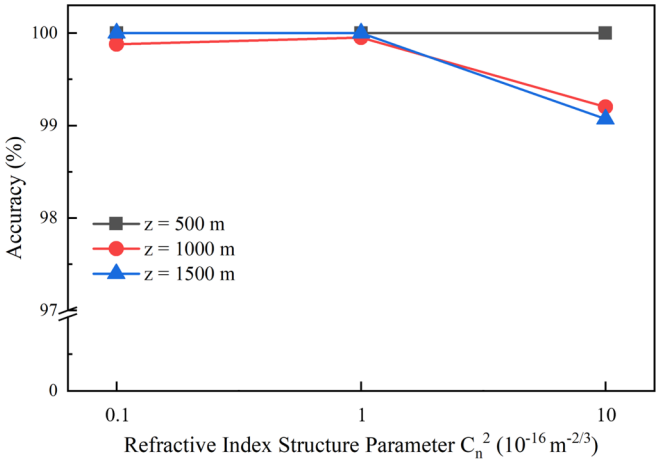

FIG. 7. Test accuracy of OAM modes for 0.1 resolution at different AT and distances.

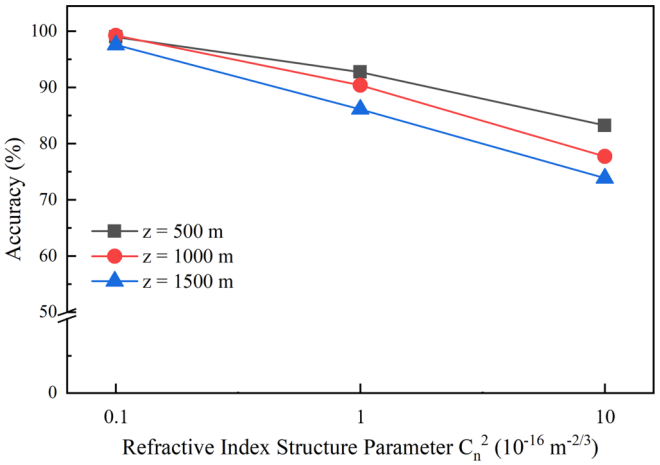

FIG. 8. Test accuracy of OAM modes for 0.01 resolution at different AT and distances.

distances. The reason might be that the diffraction patterns of fractional OAM-mode category for 0.1 resolution have been captured well by our model. Therefore, our ResNet based CNN model can accurately predict the subtle images. This is also validated at 1000 m, which also has a soft change in light distribution. Furthermore, at the longest propagation 1500 m, the test set accuracy is up to 99.07% even with strong $C_n^2 = 1 \times 10^{-15}$ $m^{-2/3}$. So, our results are remarkable for the OAM beam recognition on fractional topological charge for 0.1 resolution.

B. Classification of OAM for 0.01 resolution

We then move toward the more challenging task—identifying the modes for 0.01 resolution under AT. A total of 60 000 images were acquired; 12 000 images were allocated for the test. The test accuracy is given in Fig. 8: The black, red, and blue lines represent the short 500-m, medium 1000-m, and long 1500-m propagation distance, respectively. With the increase in distance and/or turbulence, not surprisingly, the accuracy declines more quickly. The accuracy decreases quite bit when AT increases from weak $C_n^2 = 1 \times 10^{-17}$ $m^{-2/3}$ to strong $C_n^2 = 1 \times 10^{-15}$ $m^{-2/3}$ at 1000 and 1500 m. The influence of AT intensity have more impact than the propagation distance.

With the increase in turbulence, the accuracy of 0.1 resolution is barely changed at three distances, still above 99%. But, the accuracy of 0.01 resolution clearly declines. Specifically, from weak $C_n^2 = 1 \times 10^{-17}$ $m^{-2/3}$ to intermediate $C_n^2 = 1 \times 10^{-16}$ $m^{-2/3}$, for 0.1 resolution, a maximum

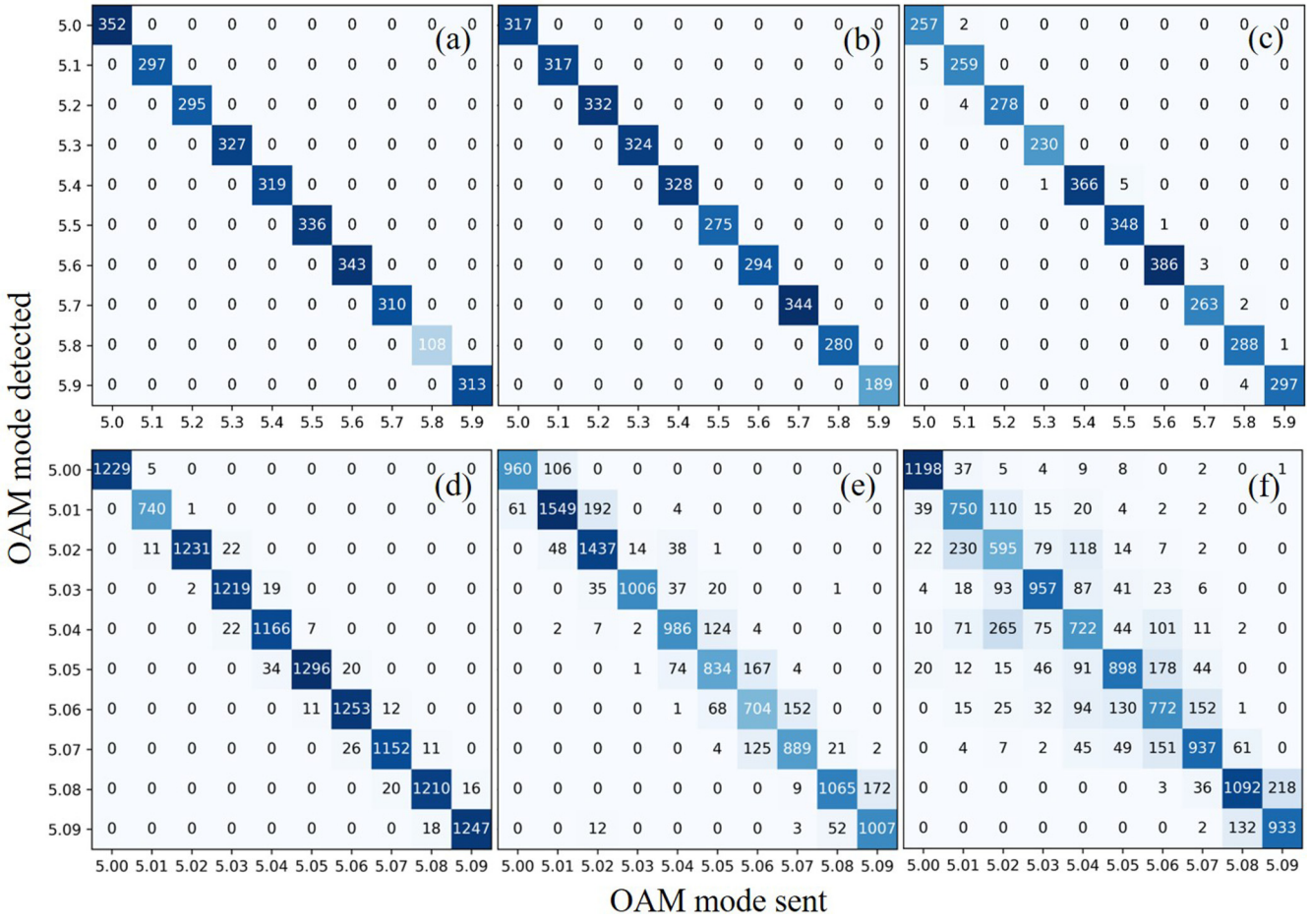

FIG. 9. Confusion matrix for 0.1 resolution (in the first row) and for 0.01 resolution (in the second row). (a), (d) Weak $C_n^2 = 1 \times 10^{-17}$ $m^{-2/3}$; (b), (e) intermediate $C_n^2 = 1 \times 10^{-16}$ $m^{-2/3}$; (c), (f) strong $C_n^2 = 1 \times 10^{-15}$ $m^{-2/3}$. The horizontal axis represents the experimental/known OAM modes, and the vertical axis presents the OAM modes being predicted. z is fixed at 1500 m.

change in accuracy is 0.07% among the three distances, but for 0.01 resolution, the accuracy declines 6.23% at 500 m, 8.83% at 1000 m, and 10.88% at 1500 m. From intermediate $C_n^2 = 1 \times 10^{-16}$ $m^{-2/3}$ to strong $C_n^2 = 1 \times 10^{-15}$ $m^{-2/3}$, for 0.1 resolution, the decline in accuracy is 0.75% at 1000 m and 0.93% at 1500 m. For 0.01 resolution, it is more, 9.51% at 500 m, 12.68% at 1000 m, and 13.20% at 1500 m. Also, the OAM crosstalk occurs to be more prominent for 0.01 than for 0.1 resolution at longer propagation distance and/or stronger AT intensity.

Figure 9 shows the confusion matrix for 0.1 resolution in the first row and 0.01 resolution in the second row. For 0.1 resolution, (a) is at weak $C_n^2 = 1 \times 10^{-17}$ $m^{-2/3}$ with accuracy 100%, (b) is at intermediate $C_n^2 = 1 \times 10^{-16}$ $m^{-2/3}$ with accuracy 100%, and (c) is at strong $C_n^2 = 1 \times 10^{-15}$ $m^{-2/3}$ with accuracy 99.07%, concerning the total number of test set 3000 at 1500 m. For 0.01 resolution, (d) is at weak $C_n^2 = 1 \times 10^{-17}$ $m^{-2/3}$ with the accuracy 97.86%, (e) is at intermediate $C_n^2 = 1 \times 10^{-16}$ $m^{-2/3}$ with accuracy 86.98%, and (f) is at strong $C_n^2 = 1 \times 10^{-15}$ $m^{-2/3}$ with accuracy 73.78%, concerning the total number of test set 12 000 at 1500 m. From the matrix of 0.1 resolution, most of the tested OAM modes are recognized correctly. In brief, the model performs extremely well in weak and intermediate turbulences, indicating that the subtle difference between adjacent modes is well identified by the CNN model. From the matrix of 0.01 resolution, there are a few mode dispersions—one mode is mistakenly detected to be the adjacent one. As the increase in AT intensity, the probability of OAM modes crosstalk is amplified, so more modes are misidentified. Still, the accuracy is remarkable, compared to the conventional methods, to resolve the similar intensity distributions of the adjacent fractional vortex modes.

VII. CONCLUSION

In conclusion, we combine experiment with theory to report high precision recognition on high-resolution (0.1 and 0.01) OAM modes in an atmosphere environment over long distance, which can be well used in Laguerre-Gaussian beams and be further expended into other kinds of vortex beams. Experimentally, a single cylindrical lens is used to transform the light distribution to have significant dark stripes, which are then learned and extracted by the ResNet based CNN model. When the fractional OAM modes ranges 5.0–5.9 at a step of 0.1, the ResNet model can identify the OAM modes with superhigh accuracy—nearly 100%—at a short propagating distance (500 m) under three turbulences (1×10^{-17} $m^{-2/3}$, 1×10^{-16} $m^{-2/3}$, 1×10^{-15} $m^{-2/3}$). At a long propagating distance (1500 m), the accuracy under weak turbulence (1×10^{-17} $m^{-2/3}$) is 100%, under intermediate turbulence (1×10^{-16} $m^{-2/3}$) is 100%, and under strong turbulence (1×10^{-15} $m^{-2/3}$) is 99.07%. For OAM modes from 5.00 to 5.09 at a step of 0.01, the accuracy under weak turbulence (1×10^{-17} $m^{-2/3}$) is still high, 98.97% at 500 m and 97.86% at 1500 m. Under intermediate turbulence $C_n^2 = 1 \times 10^{-16}$ $m^{-2/3}$, the accuracy remains high, 92.74% at 500 m and 86.98% at 1500 m. Under strong turbulence $C_n^2 = 1 \times 10^{-15}$ $m^{-2/3}$, the accuracy is decent, 83.23% at 500 m and 73.78% at 1500 m.

In the future, one way to expand recognition of fractional OAM modes is to encode the grayscale value of images using different OAM modes at 0.01 resolution to build a superhigh-resolution multiplexing system, and experimentally verify its performance. This scheme can then be modeled by sophisticated deep learning algorithms to improve the communication capacity of coding upon combining wavelength-division multiplexing and polarization multiplexing [15,51].

ACKNOWLEDGMENTS

This work was supported by the National Natural Science Foundation of China (Grants No. 12174115, No. 91836103, and No. 11834003) and a Joint Physics Research Institute Challenge grant of the NYU-ECNU Institute of Physics at NYU Shanghai.

[1] L. Allen, M. W. Beijersbergen, R. J. C. Spreeuw, and J. P. Woerdman, Orbital angular momentum of light and the transformation of laguerre-gaussian laser modes, Phys. Rev. A **45**, 8185 (1992).

[2] A. Forbes, A. Dudley, and M. McLaren, Creation and detection of optical modes with spatial light modulators, Adv. Opt. Photonics **8**, 200 (2016).

[3] M. J. Padgett, Orbital angular momentum 25 years on, Opt. Express **25**, 11265 (2017).

[4] Y. J. Shen, X. J. Wang, Z. W. Xie, C. J. Min, X. Fu, Q. Liu, M. L. Gong, and X. C. Yuan, Optical vortices 30 years on: OAM manipulation from topological charge to multiple singularities, Light: Sci. Appl. **8**, 90 (2019).

[5] G. Molina-Terriza, J. P. Torres, and L. Torner, Twisted photons, Nat. Phys. **3**, 305 (2007).

[6] M. Erhard, R. Fickler, M. Krenn, and A. Zeilinger, Twisted photons: new quantum perspectives in high dimensions, Light: Sci. Appl. **7**, 17146 (2018).

[7] M. Padgett and R. Bowman, Tweezers with a twist, Nat. Photonics **5**, 343 (2011).

[8] S. C. Chapin, V. Germain, and E. R. Dufresne, Automated trapping, assembly, and sorting with holographic optical tweezers, Opt. Express **14**, 13095 (2006).

[9] F. Tamburini, G. Anzolin, G. Umbriaco, A. Bianchini, and C. Barbieri, Overcoming the Rayleigh Criterion Limit with Optical Vortices, Phys. Rev. Lett. **97**, 163903 (2006).

[10] Z. Y. Zhou, D. S. Ding, Y. K. Jiang, Y. Li, S. Shi, X. S. Wang, and B. S. Shi, Orbital angular momentum light frequency conversion and interference with quasi-phase matching crystals, Opt. Express **22**, 20298 (2014).

[11] A. Forbes, M. de Oliveira, and M. R. Dennis, Structured light, Nat. Photonics **15**, 253 (2021).

[12] J. Wang, J. Y. Yang, I. M. Fazal, N. Ahmed, Y. Yan, H. Huang, Y. X. Ren, Y. Yue, S. Dolinar, M. Tur, and A. E. Willner, Terabit free-space data transmission employing orbital angular momentum multiplexing, Nat. Photonics **6**, 488 (2012).

[13] M. Krenn, R. Fickler, M. Fink, J. Handsteiner, M. Malik, T. Scheidl, R. Ursin, and A. Zeilinger, Communication with spatially modulated light through turbulent air across vienna, New J. Phys. **16**, 113028 (2014).

[14] A. Trichili, A. B. Salem, A. Dudley, M. Zghal, and A. Forbes, Encoding information using laguerre gaussian modes over free space turbulence media, Opt. Lett. **41**, 3086 (2016).

[15] A. E. Willner, Z. Zhao, C. Liu, R. Z. Zhang, H. Q. Song, K. Pang, K. Manukyan, H. Song, X. Z. Su, G. D. Xie, Y. X. Ren, Y. Yan, M. Tur, A. F. Molisch, R. W. Boyd, H. B. Zhou, and N. Z. Hu, A. Minoofar, and H. Huang, Perspectives on advances in high-capacity, free-space communications using multiplexing of orbital-angular-momentum beams, APL Photonics **6**, 030901 (2021).

[16] J. Wang, J. Liu, S. H. Li, Y. F. Zhao, J. Du, and L. Zhu, Orbital angular momentum and beyond in free- space optical communications, Nanophononics **11**, 645 (2022).

[17] M. V. Berry, Optical vortices evolving from helicoidal integer and fractional phase steps, J. Opt. A: Pure Appl. Opt. **6**, 259 (2004).

[18] W. M. Lee, X. C. Yuan, and K. Dholakia, Experimental observation of optical vortex evolution in a gaussian beam with an embedded fractional phase step, Opt. Commun. **239**, 129 (2004).

[19] J. Leach, E. Yao, and M. J. Padgett, Observation of the vortex structure of a non-integer vortex beam, New J. Phys. **6**, 71 (2004).

[20] N. Zhang, J. A. Davis, I. Moreno, J. Lin, K. J. Moh, D. M. Cottrell, and X. C. Yuan, Analysis of fractional vortex beams using a vortex grating spectrum analyzer, Appl. Opt. **49**, 2456 (2010).

[21] H. C. Huang, Y. T. Lin, and M. F. Shih, Measuring the fractional orbital angular momentum of a vortex light beam by cascaded mach-zehnder interferometers, Opt. Commun. **285**, 383 (2012).

[22] P. Y. Li, B. Wang, X. B. Song, and X. D. Zhang, Non-destructive identification of twisted light, Opt. Lett. **41**, 1574 (2016).

[23] J. Zhu, P. Zhang, D. Z. Fu, D. X. Chen, R. F. Liu, Y. N. Zhou, H. Gao, and F. L. Li, Probing the fractional topological charge of a vortex light beam by using dynamic angular double slits, Photonics Res. **4**, 187 (2016).

[24] G. C. Berkhout, M. P. Lavery, J. Courtial, M. W. Beijersbergen, and M. J. Padgett, Efficient Sorting of Orbital Angular Momentum States of Light, Phys. Rev. Lett. **105**, 153601 (2010).

[25] B. Berger, M. Kahlert, D. Schmidt, and M. Assmann, Spectroscopy of fractional orbital angular momentum states, Opt. Express **26**, 32248 (2018).

[26] S. N. Alperin, R. D. Niederriter, J. T. Gopinath, and M. E. Siemens, Quantitative measurement of the orbital angular momentum of light with a single, stationary lens, Opt. Lett. **41**, 5019 (2016).

[27] D. Deng, M. C. Lin, Y. Li, and H. Zhao, Precision Measurement of Fractional Orbital Angular Momentum, Phys. Rev. Appl. **12**, 014048 (2019).

[28] H. Zhang, J. Zeng, X. Y. Lu, Z. Y. Wang, C. L. Zhao, and Y. J. Cai, Review on fractional vortex beam, Nanophotonics **11**, 241 (2022).

[29] L. F. Zhang, Y. Y. Lin, Y Z, Z. H. Huang She, J. Z. Li, X. J. Luo, H. Yan, W. Huang, D. W. Zhang, and S. L. Zhu, Recognition of orbital-angular-momentum modes with different topological charges and their unknown superpositions via machine learning, Phys. Rev. A **104**, 053525 (2021).

[30] A. S. Razavian, H. Azizpour, J. Sullivan, and S. Carlsson, CNN features off-the-shelf: An astounding baseline for recognition, *2014 IEEE Conference on Computer Vision and Pattern Recognition Workshops* (IEEE, 2014), pp. 512-519.

[31] T. Doster and A. T. Watnik, Machine learning approach to OAM beam demultiplexing via convolutional neural networks, Appl. Opt. **56**, 3386 (2017).

[32] Z. W. Liu, S. Yan, H. G. Liu, and X. F. Chen, Superhigh-resolution Recognition of Optical Vortex Modes Assisted by a Deep-Learning Method, Phys. Rev. Lett. **123**, 183902(2019).

[33] Y. B. Na and D. K. Ko, Deep-learning-based high-resolution recognition of fractional-spatial-mode-encoded data for free-space optical communications, Sci. Rep. **11**, 2678 (2021).

[34] F. Tamburini, E. Mari, A. Sponselli, B. Thide, A. Bianchini, and F. Romanto, Encoding many channels on the same frequency through radio vorticity: First experimental test, New J. Phys. **14**, 033001 (2012).

[35] G. Vallone, V. D'Ambrosio, A. Sponselli, S. Slussarenko, L. Marrucci, F. Sciarrino, and P. Villoresi, Free-space Quantum Key Distribution by Rotation-Invariant Twisted Photons, Phys. Rev. Lett. **113**, 060503 (2014).

[36] M. P. Lavery, B. Heim, C. Peuntinger, O. S. Magana-Loaiza, E. Karimi, T. Bauer, P. Banzer, C. Marquardt, A. E. Willner, R. W. Boyd, M. J. Padgett, and G. Leuchs, Study of turbulence induced orbital angular momentum channel crosstalk in a 1.6 km free-space optical link, in *CLEO: Science and Innovations* (Optical Society of America, 2015), paper STu1L4.

[37] M. Krenn, J. Handsteiner, M. Fink, and A. Zeilinger, Twisted light transmission over 143 km, Proc. Natl. Acad. Sci. USA **113**, 13648 (2016).

[38] Y. Xia and J. P. Yin, Generation of a focused hollow beam by an phase plate and its applications in atom or molecule optics, J. Opt. Soc. Am. B **22**, 529 (2005).

[39] J. P. Yin, W. J. Gao, and Y. F. Zhu, Generation of dark hollow beams and their applications, Prog. Opt. **45**, 119 (2003).

[40] G. Molina-Terriza, J. Recolons, J. P. Torres, and L. Torner, Observation of the Dynamical Inversion of the Topological Charge of an Optical Vortex, Phys. Rev. Lett. **87**, 023902 (2001).

[41] V. H. Denisenko, M. S. Soskin, and M. V. Vasnetsov, Transformations of laguerre-gaussian modes carrying optical vortex and their orbital angular momentum by cylindrical lens, Proc SPIE **4607**, 54 (2002).

[42] X. Fang, Z. Kuang, P. Chen, H. Yang, Q. Li, W. Hu, Y. Lu, Y. Zhang, and M. Xiao, Examining second-harmonic generation of high-order laguerre–gaussian modes through a single cylindrical lens, Opt. Lett. **42**, 4387 (2017).

[43] L. C. Andrews, An analytical model for the refractive index power spectrum and its application to optical scintillations in the atmosphere, J. Mod. Opt. **39**, 1849 (1992).

[44] L. C. Andrews and R. L. Phillips, *Laser Beam Propagation through Random Media* (SPIE, Bellingham, Washington, USA, 2005).

[45] J. I. Davis, Consideration of atmospheric turbulence in laser systems design, Appl. Opt. **5**, 139 (1966).

[46] S. M. Zhao, J. Leach, L. Y. Gong, J. Ding, and B. Y. Zheng, Aberration corrections for free-space

optical communications in atmosphere turbulence using orbital angular momentum states, Opt. Express **20**, 452 (2012).

[47] A. D. McAulay, Generating kolmogorov phase screens for modeling optical turbulence, Proc. SPIE **4034**, 50 (2000).

[48] K. M. He and J. Sun, Convolutional neural networks at constrained time cost, 2015 *IEEE Conference on Computer Vision and Pattern Recognition*, Boston, June (IEEE, 2015).

[49] T. Akiba, S. Suzuki, and K. Fukuda, Extremely large minibatch SGD: training ResNet-50 on ImageNet in 15 minutes, arXiv:1711.04325.

[50] K. M. He, X. Y. Zhang, S. Q. Ren, and J. Sun, Deep residual learning for image recognition, *Proceedings of the IEEE Conference on Computer Vision and Pattern Recognition*, Las Vegas, June (IEEE, 2016).

[51] A. E. Willner, K. Pang, H. Song, K. H. Zou, and H. B. Zhou, Orbital angular momentum of light for communications, Appl. Phys. Rev. **8**, 041312 (2021).